Reverse Monte Carlo modelling of amorphous $Si_3B_3N_7$ using scattering and ^{15}N NMR data

Reverse Monte Carlo modelling of amorphous $Si_3B_3N_7$ using scattering and ^{15}N NMR data

Markus Doerr and Christel M Marian

Institut für Theoretische Chemie und Computerchemie, Heinrich–Heine–Universität Düsseldorf, Universitätsstraße 1, 40225 Düsseldorf, Germany

E-mail: Markus.Doerr@uni-duesseldorf.de and Christel.Marian@uni-duesseldorf.de

Abstract

We present an enhanced reverse Monte Carlo approach that includes fitting to NMR data in the form of chemical shifts in addition to the usually used scattering data. Furthermore, the internal energy is accounted for in the cost function to prevent unphysical structures. This approach was applied to generate structural models of amorphous $Si_3B_3N_7$, which is a prototype of a new class of high performance ceramics exhibiting interesting features like high thermal and mechanical stability.

We fitted our structural models in direct space to radial distribution functions from x-ray, neutron and electron scattering experiments, and to the ^{15}N NMR spectrum of the ceramic. This spectrum could not be interpreted before since it exhibits a broad structureless signal which is a superposition of peaks related to different chemical environments NB_xSi_{3-x} ($x = 0$–3) whose chemical shifts were only partly known experimentally. Therefore we based the calculation of NMR data in the reverse Monte Carlo optimizations on previous theoretical work that was done in our group. All generated models reproduce the experimental radial distribution functions very well. This good agreement does not deteriorate when the NMR data are taken into account. Fitting the models to ^{15}N NMR chemical shifts in addition to scattering data results in structural changes that not only improve the agreement with the experimental magic-angle spinning (MAS) NMR spectrum but yield also significantly better second-nearest neighbour coordination statistics.

M Supplementary data are available from stacks.iop.org/JPhysCM/19/056201

1. Introduction

Amorphous multinary nitrides of silicon and boron such as a-$Si_3B_3N_7$ or a-$SiBN_3C$ [1–3] are a relatively new class of high performance materials that exhibit very promising thermal and mechanical properties. The ternary ceramic a-$Si_3B_3N_7$, for example, is stable up to ≈1900 K, when decomposition sets in. Even more stable against thermal decomposition ($T_{dec} \approx 2100$ K)

is a-SiBN$_3$C. Both materials are also surprisingly stable in oxidizing atmosphere. In addition to their thermal stability these materials exhibit good creep resistance and tensile strength.

For a better understanding of the origin of these fascinating properties it is highly desirable to gain insight into the microscopic structure. However, for amorphous compounds such as the above ones, structural information is very difficult to extract from experiment. For example, scattering methods—very powerful tools for detailed structure exploration of crystalline solids—only yield spatially averaged information when applied to amorphous systems, basically limited to the first one or two coordination spheres.

Because of the experimental difficulties, theoretical methods play an important role for structure elucidation of amorphous materials. These methods comprise a large spectrum ranging from molecular dynamics (on *ab initio* [4] or empirical potential energy surfaces [5, 6]) or Monte Carlo methods [6, 7] to rule-based methods for building up continuous random networks [8, 9]. In addition, quantum chemical calculations on molecules or clusters can be applied for finding relations between structure and experimental properties [10, 11] or for examining reactions occurring during synthesis of the materials [12].

The reverse Monte Carlo (RMC) method [13, 14], which is used in this work, is an *in silico* method that is somewhat different from the previously described methods as it connects theoretical modelling and experimental data. It combines information from different experimental sources for generating structural models with atomic resolution that are in agreement with all this information. One of the shortcomings of the reverse Monte Carlo method is the ambiguity of the generated models, which is owing to the limited structural information in the experimental data. To overcome these ambiguities it is important to use as much experimental information as possible, preferably from different experimental sources. Inclusion of NMR data is a step in this direction.

There has already been some work on using NMR data in RMC optimizations. Zwanziger *et al* fitted their models to the second moment of the magnetic dipole interaction between two nuclei and used information about coordination numbers obtained from NMR [15, 16]. The second moment of the dipole interaction can easily be calculated from the partial radial distribution functions which are a by-product of the scattering-data calculation. In this work we pursue a different approach that focuses on the NMR chemical shifts which are calculated as a function of the composition and the geometry of the first coordination sphere. This will be illustrated in more detail in section 2.2.2.

Our modelling approach is restricted to the simpler ternary nitride a-Si$_3$B$_3$N$_7$. This restriction has two reasons: firstly, the stoichiometric composition of a-Si$_3$B$_3$N$_7$ is well defined, in contrast to, e.g., a-SiBN$_3$C, where one finds a greater spread of compositions. Secondly, the modelling of a ternary amorphous system is already quite difficult and the level of difficulty grows with increasing number of constituents.

Several *in silico* approaches for modelling of a-Si$_3$B$_3$N$_7$ have already been reported in the literature [4–7, 17–19]. Some of these approaches include a final RMC refinement of the structures, where the models were fitted to scattering data from two different experiments (x-ray and neutron). In this paper we are going to present RMC models of a-Si$_3$B$_3$N$_7$ that were fitted to data from three different scattering experiments (x-ray, neutron, and electron) and in addition to the ^{15}N NMR spectrum of the ceramic.

Amorphous Si$_3$B$_3$N$_7$ was extensively examined experimentally. X-ray [20], neutron [20, 21] and electron scattering [22] experiments were performed, partially on isotopically enriched samples, yielding the pair distribution functions (PDFs) of the material. Electron radiation was also used to determine the element distribution of the material by energy filtered transmission electron microscopy (EFTEM) [22]. The latter experiment revealed a homogeneous distribution of the elements Si, B, and N at length scales larger than $\approx$10 Å.

^{29}Si, ^{11}B, and ^{15}N MAS NMR experiments were performed to examine the compositions of the first coordination spheres [23]. From the ^{11}B and ^{29}Si spectra it could be concluded by comparison with crystalline reference substances that the material is composed of trigonal planar BN_3 units and distorted tetrahedral SiN_4 units, which is in agreement with the coordination numbers determined from the PDFs. A similar interpretation of the ^{15}N NMR spectrum, which exhibits a broad structureless peak ranging over $\approx$100 ppm, was not possible. This peak is presumably a superposition of signals related to different coordination environments NB_xSi_{3-x} (x = 0–3). A determination of the relative fractions of these environments was mainly hindered by the fact that crystalline reference substances exist only for homogeneous coordination environments NB_3 and NSi_3. Nuclear magnetic resonance techniques were also applied to examine the structure beyond the first coordination spheres. The numbers of second-nearest neighbours of Si and B were determined in a series of double resonance NMR experiments [24]. From these data, information about preferred connection schemes of the BN_3 and SiN_4 units could be extracted.

The uninterpretable ^{15}N NMR spectrum of the ceramic motivated several theoretical investigations in our group that should lead to a better understanding of the spectrum and of the structure of a-$Si_3B_3N_7$. The idea was to perform quantum chemical calculations of the chemical shifts for (a) finding relations between the structure and the chemical shift and (b) determining the unknown chemical shifts in NB_2Si and $NBSi_2$ environments in the solid state. From calculations of the chemical shifts in NB_3 and NB_4 environments it was possible to develop a parameterization that relates the N chemical shift to the mean distance of the next (and second to next) neighbours [11]. Calculations on cluster models of β-Si_3N_4 were performed to examine the nitrogen chemical shifts in NSi_3 environments [25, 26]. The *ab initio* calculations were able to reproduce the chemical shifts of the two crystallographically different N atoms in β-Si_3N_4, but no simple structure–property relationships could be derived in this case. And finally, the previously unknown chemical shifts in mixed environments NB_2Si and $NBSi_2$ in the solid state were determined using cluster models of hypothetical crystalline $Si_3B_3N_7$ [27]. The work that is presented in this paper makes use of the knowledge assembled in all this theoretical work as well as in the experimental work done by other groups.

2. Theory and methods

2.1. Reverse Monte Carlo

The RMC algorithm [13, 14] is a method for generating structural models that are consistent with a set of experimental data. Consistency is achieved by minimizing a cost function (CF) which measures the deviation between the experimental data and the data calculated from the model (equation (1)).

$$CF = \sum_{i=1}^{N} \left[{}^{calc}G(r_i) - {}^{exp}G(r_i) \right]^2 \tag{1}$$

N is the number of data points, ^{exp}G and ^{calc}G are the experimental and calculated data. Typically the data consist of radial distribution functions $G(r)$ or structure factors $S(Q)$. In our approach they may also be the intensity $I(\delta)$ of an NMR spectrum. In the RMC procedure the cost function is minimized by repeated random modification (usually the random move of a single atom) of the structural model. After each move the difference between the cost functions of the new and the previous configuration $\Delta CF = CF_{new} - CF_{old}$ is calculated and, depending on the value of ΔCF, the move is either accepted or rejected. As in every global optimization one has to take care that the system is not trapped in local minima. This is achieved by applying an

acceptance criterion which is very similar to the one that is used in ordinary Metropolis Monte Carlo simulations (equation (2)).

$$\text{acceptance if } \exp -\frac{\Delta CF}{\sigma} \leqslant RND[0\ldots1]. \tag{2}$$

RND[0...1] is a random number between 0 and 1. Using this criterion, uphill moves ($\Delta CF > 0$) are accepted with a probability that is high for small ΔCF and low for large ΔCF. Downhill moves are always accepted. The parameter σ controls the acceptance probability of uphill moves. Several variations of equation (2) can be found in the literature. In the original RMC implementation, for example, σ is replaced by 2 and the right-hand side of equation (1) contains a factor $1/\sigma^2(r_i)$, where $\sigma(r_i)$ represents the experimental error. If σ is not kept constant during the optimization, a simulated annealing procedure [28, 29] can be achieved by stepwise lowering σ. Several factors σ_i can then be used for separately controlling parts of the cost function belonging to different experiments. Further details of the cost function applied in the present work are described in section 2.2.5.

2.2. Details of the calculations

2.2.1. Experimental scattering data. All models were optimized with respect to radial distribution functions (RDFs) $G(r)$ from x-ray, neutron and electron scattering experiments [20, 22]. It turned out that the electron scattering RDF was not properly scaled, probably because of multiple scattering present in the data, which is a common problem in electron scattering experiments. To obtain properly scaled data we performed RMC optimizations fitting the model to x-ray, neutron and the original electron scattering data. After these optimizations we rescaled the experimental electron scattering data minimizing the difference between calculated and experimental data. The rescaled electron scattering data were used in all subsequent optimizations.

During the RMC runs all RDFs were calculated directly from the atomic positions. This results in slightly broadened RDFs because the experimental radial distribution functions are artificially broadened due to finite integration limits applied in the Fourier transform of the scattering intensity. The artificial broadening of the experimental RDFs is different in the three scattering experiments because the experimentally accessible ranges of the scattering intensities were not identical. The scattering intensity could be detected up to 26 Å^{-1} (x-ray scattering), 50 Å^{-1} (neutron scattering) and 30 Å^{-1} (electron scattering). From our experience the broadening of the model RDFs due to calculation of the scattering data in real space is quite small though for amorphous systems [30]. Another disadvantage of calculating the radial distribution functions directly from the atomic positions is the possible generation of artificial structural features by fitting to ghost peaks in the experimental data which are also a side effect of the finite Fourier transform of the scattering intensity. But as can be seen in the following sections, this problem did not arise in our calculations. Despite these principal problems, calculation of the RDFs directly from the atomic positions greatly enhances the computing speed by avoiding two Fourier transforms (one for calculation of the scattering intensity from the atomic positions, and one for calculation of the RDF from the scattering intensity), thus making much longer optimizations possible.

2.2.2. NMR data. As already mentioned in the introduction, the ^{15}N NMR spectrum of a-Si$_3$B$_3$N$_7$ is a superposition of signals related to different chemical environments NB$_x$Si$_{3-x}$ ($x = 0$–3) [23]. Only the chemical shifts in homogeneous environments NB$_3$ and NSi$_3$ could be determined experimentally using crystalline reference substances. Jeschke and Hoffbauer
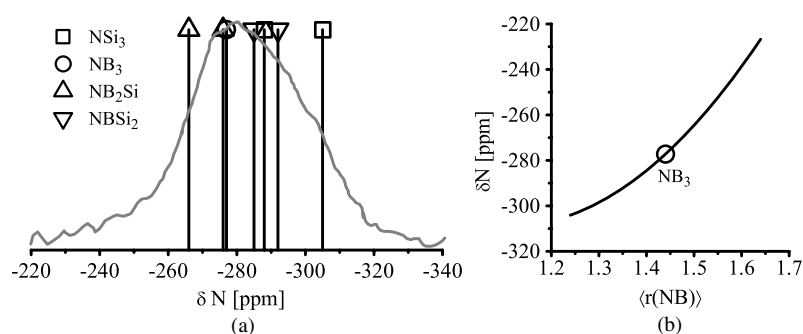
Figure 1. N chemical shifts as used in RMC optimizations. (a) Chemical shifts in different threefold coordinated nitrogen environments and ^{15}N NMR spectrum of a-$Si_3B_3N_7$ [23]. (b) Distance dependence of chemical shifts in NB_3 environments. $\langle r_{NB} \rangle$ is the mean distance of the first neighbours. The symbol marks the shift at calculated equilibrium distance of the model used in [11]. All chemical shifts are relative to liquid CH_3NO_2.

measured the ^{15}N chemical shifts of crystalline hexagonal and cubic boron nitride and found values of -280 ppm for NB_3 and -359 ppm for NB_4 environments relative to CH_3NO_2 [31]. Harris *et al* determined the ^{15}N chemical shifts in α- and β-Si_3N_4 as -309, -307, -297 and -285 ppm for the four crystallographically different nitrogen atoms in α-Si_3N_4 and -307 and -290 ppm for the two crystallographically different nitrogen atoms in β-Si_3N_4 [32].

The nitrogen chemical shifts of hexagonal and cubic boron nitride and in β-Si_3N_4 were also examined in our group using computational methods [10, 11, 25, 26]. For chemical shifts in NB_3 and NB_4 environments it was possible to develop a parameterization which relates the chemical shift to the local structure (the mean distance of the first- and second-nearest neighbour atoms). With this parameterization a chemical shift of -287 ppm at equilibrium distance is computed for NB_3 environments. The dependence of the chemical shift on the mean first-neighbour distances is shown in figure 1(b). Chemical shifts in β-Si_3N_4 were calculated as -298 and -315 ppm. Because the chemical shifts in mixed environments NB_2Si and $NBSi_2$ in the solid state are not known experimentally, we had performed calculations using clusters of hypothetical crystalline $Si_3B_3N_7$ polymorphs suggested by Kroll and Hoffmann [33] and had found values between -272 and -290 ppm for NB_2Si and -293 and -302 ppm for $NBSi_2$ environments (referring to the central atoms of the clusters) [27]. Contrary to previous assumptions, the chemical shift of the threefold coordinated N thus does not steadily increase with the number of Si neighbours. No correlations between variations of the local structure and the chemical shifts could be found for the latter three nitrogen environments.

Using the available data, we calculated the nitrogen chemical shifts primarily as a function of the coordination environments. Chemical shifts in NB_3 and NB_4 environments were calculated using the parameterization against the mean distances of the first neighbours from [11]. For consistency, all calculated chemical shifts were based on theoretical data. Our first attempt was to use the original values of -287 ppm for NB_3 (at a distance of 1.44 Å), -276 and -286 ppm for NB_2Si, -295 and -302 ppm for $NBSi_2$ and -298 and -315 ppm for NSi_3 environments. However, because experience had shown that the calculated chemical shifts are systematically too negative, we corrected for these errors by moving all shifts by $+10$ ppm. The resulting chemical shifts (-277 ppm for NB_3, -286 and -296 ppm for NB_2Si, -305 and -312 ppm for $NBSi_2$ and -288 and -305 ppm for NSi_3) are shown in figure 1(a). As can be seen, all shifts are within the range of the peak in the experimental ^{15}N NMR spectrum now. To

account for uncertainties inherent in this approach all chemical shifts (including those of NB_3 environments) were broadened by Gaussians with a standard deviation of 5 ppm, corresponding to a full width at half maximum of 11.8 ppm. It should be noted that the chemical shifts in NSi_3 environments, although based on calculations only on β-Si_3N_4, cover the range of shifts measured in α-Si_3N_4 and in β-Si_3N_4.

For the fitting procedure the area of the experimental peak was normalized to 1. Likewise the areas of all calculated peaks for threefold coordinated atoms were chosen to sum up to 1. This implies that nitrogen environments in the model which were different from the ones included in the parameterization, for instance under- or over-coordinated N atoms, increased the deviation between calculated and experimental NMR data and thus gave rise to a penalty term. The coordination environments were determined using element-pair specific distance thresholds.

It should be noted that the parameterization of the chemical shifts used in these calculations is quite crude because the chemical shifts are primarily calculated as a function of the coordination environment. It would be highly desirable to have parameterizations of the chemical shifts in the solid state available that allow for better consideration of structural effects on the chemical shifts. These are not available at present, however. Our current approach is similar to the common practice of interpreting experimental NMR data by simulation of the spectrum as a superposition of Gaussians representing different chemical environments as it is implemented, for example, in the DMFIT program [34]. In our procedure this fitting to the experimental spectrum is coupled to fitting to other experimental data which should improve the reliability of the results.

2.2.3. Potential energy. In addition to the terms related to differences between calculated and experimental data we incorporated the potential energy as an additional part of the cost function. This should prevent the generation of physically unrealistic structures like under- and over-coordinated atoms or highly strained coordination environments. The potential energy was calculated from a computationally efficient two-body potential developed in our group [35]. This potential is based on experimental and *ab initio* solid state and diatomic molecular data of compounds containing Si, B, and N atoms. It successfully reproduces experimental data regarding structural properties such as bond lengths and bulk properties, e.g. vibrational frequencies of the binary compounds BN and Si_3N_4 with threefold coordinated B and N atoms and fourfold coordinated Si atoms.

2.2.4. Starting structure. We used a structural model of hypothetical crystalline $\beta 2$-$Si_3B_3N_7$ with 702 atoms (composition $Si_{162}B_{162}N_{378}$) in a periodically repeated cubic box with side length $L = 19.7$ Å. Prior to RMC optimization the structure was amorphized by melting it in a molecular dynamics (MD) run (several nanoseconds at 3500 K, *NVT*-ensemble) [36]. The structure resulting from this MD run still exhibits a certain degree of structural order. This can be seen in figure 2, where the tubes along the z-axis, which are typical for the crystalline structure, are still visible. The relatively sharp peaks of the radial distribution functions of the starting structure (figures 3(a)–5(a)) also indicate a high degree of ordering.

2.2.5. Optimization procedure. The optimization procedure followed a simulated annealing protocol, where the temperature factor T (see equations (3)–(5)) was lowered in 15 steps from a high starting value to a final temperature of 0 which corresponds to a local optimization. Each temperature was kept constant for 6 000 000 atomic movements (about 8500 Monte Carlo cycles), allowing the system to equilibrate and to wander around on the cost function surfaces.
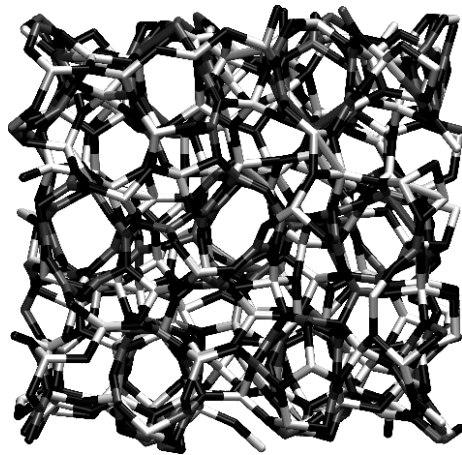
Figure 2. Starting structure, view along z-axis of the simulation cell. N: black; B: medium grey; Si: light grey.
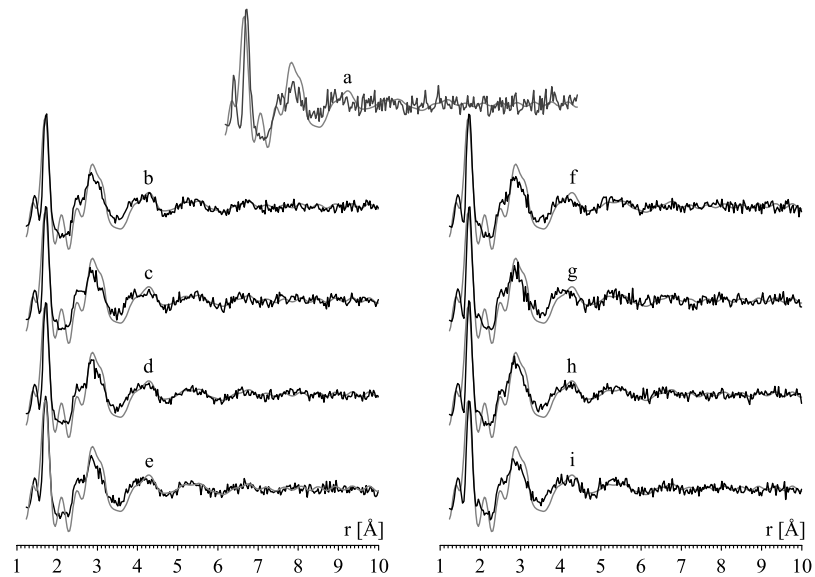

Figure 3. X-ray scattering pair correlation functions $G(r)$ of optimized models (black) and experimental data (grey) [20]. For comparison data calculated from the starting structure are also shown. (a) Starting structure; (b)–(e) class A models (optimized with respect to scattering and NMR data); (f)–(i) class B models (optimized only with respect to scattering data).

Five cost functions were employed in the RMC optimization: one for the potential energy (equation (3)), three corresponding to three different scattering experiments (equation (4)) and one related to NMR data (equation (5)). After each Monte Carlo move acceptance tests were performed for all five cost functions, separately evaluating the following expressions.

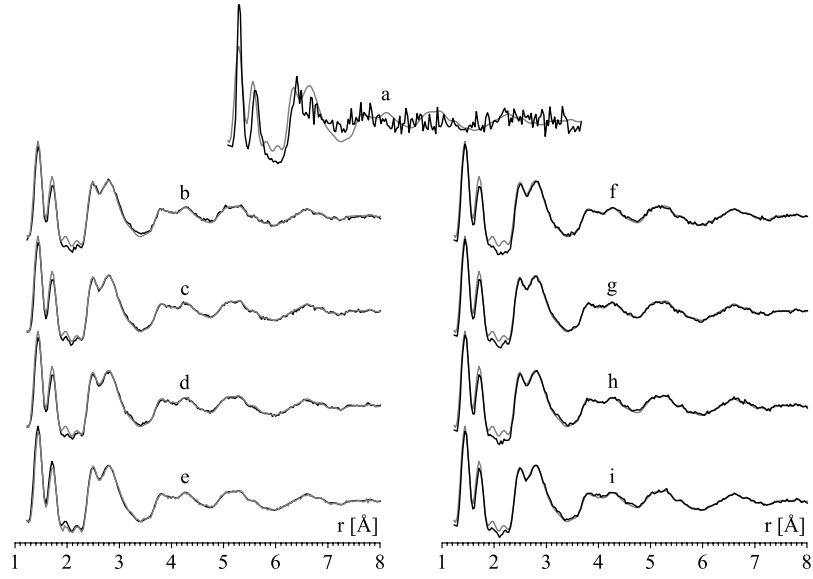$$\exp-\frac{\Delta E}{k_{\mathrm{E}}T} \tag{3}$$

Figure 4. Neutron scattering pair correlation functions $G(r)$ of optimized models (black) and experimental data (grey) [20]. For comparison data calculated from the starting structure are also shown. (a) Starting structure; (b)–(e) class A models (optimized with respect to scattering and NMR data); (f)–(i) class B models (optimized only with respect to scattering data).

Figure 5. Electron scattering pair correlation functions $G(r)$ of optimized models (black) and experimental data (grey) [22]. For comparison data calculated from the starting structure are also shown. (a) Starting structure; (b)–(e) class A models (optimized with respect to scattering and NMR data); (f)–(i) class B models (optimized only with respect to scattering data).
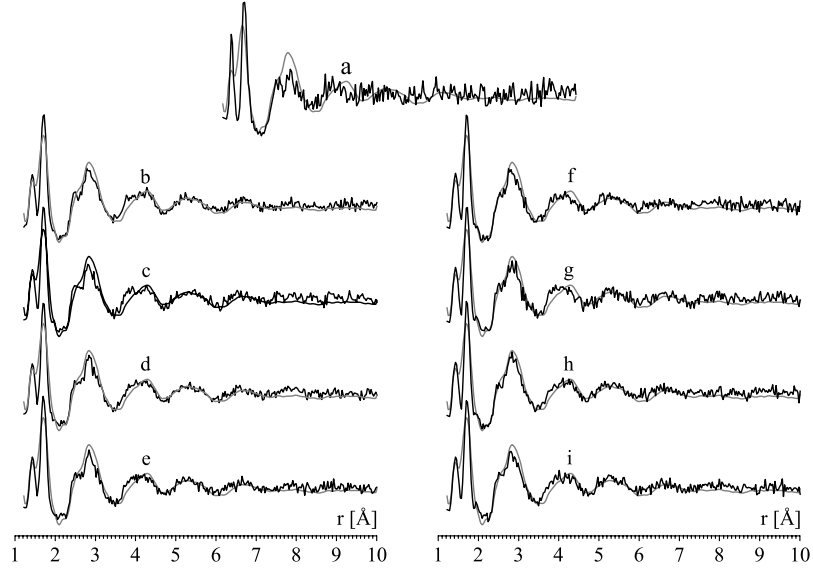
$$\exp-\frac{\Delta\mathrm{CF_X}}{k_X T}; \qquad \mathrm{CF_X} = \sum_{i=1}^{N} \left[{}^{\mathrm{calc}}G_X(r_i) - {}^{\mathrm{exp}}G_X(r_i) \right]^2 \qquad (4)$$

$(X = \text{x-ray, neutron, electron})$.

Table 1. Weighting factors k used in RMC optimizations. The calculations are labelled according to figures 3–9.

Label	k_E	k_{x-ray}	$k_{neutron}$	$k_{electron}$	k_{NMR}
		Class A: optimization with respect to scattering and NMR data			
(b)	5.17041×10^{-4}	9.10187×10^{-3}	6.65760×10^{-4}	6.27161×10^{-3}	4.66722×10^{-9}
(c)	5.17041×10^{-4}	9.10187×10^{-3}	3.32880×10^{-4}	6.27161×10^{-3}	4.66722×10^{-9}
(d)	5.17041×10^{-4}	6.82641×10^{-3}	4.99320×10^{-4}	4.70371×10^{-3}	3.50042×10^{-9}
(e)	5.17041×10^{-4}	6.82641×10^{-3}	2.49660×10^{-4}	4.70371×10^{-3}	3.50042×10^{-9}
		Class B: optimization only with respect to scattering data			
(f)	5.17041×10^{-4}	1.44797×10^{-2}	1.03999×10^{-3}	9.91237×10^{-3}	—
(g)	5.17041×10^{-4}	1.44797×10^{-2}	0.52000×10^{-3}	9.91237×10^{-3}	—
(h)	5.17041×10^{-4}	0.96531×10^{-2}	0.69333×10^{-3}	6.60825×10^{-3}	—
(i)	5.17041×10^{-4}	0.96531×10^{-2}	0.34666×10^{-3}	6.60825×10^{-3}	—

$$\exp -\frac{\Delta CF_{NMR}}{k_{NMR}T}; \qquad CF_{NMR} = \sum_{i=1}^{N} \left[{}^{calc}I_{NMR}(\delta_i) - {}^{exp}I_{NMR}(\delta_i) \right]^2. \qquad (5)$$

A move was only accepted if all acceptance tests were positive, i.e. if all of the exponential terms in equations (3)–(5) were $\leqslant$ RND[0...1]. The parameters k_X thus control how freely the system can move on the different cost function surfaces. They may also be regarded as weighting factors of the different cost functions.

Our acceptance criterion is different from the usual approach where the acceptance test is applied to a weighted sum of the cost functions. We decided to use this acceptance criterion because experience has shown that with our form the different cost functions are more easily controllable [30]. For example, if the acceptance test is only applied to the sum of the cost functions, an increase of the potential energy may be compensated by a decrease of other cost functions, resulting in unrealistic structures with high energy.

For finding values for k_E, k_X, and k_{NMR} in equations (3)–(5) that resulted in models with not too high an energy and fitting similarly well to all experimental data, a series of shorter RMC optimizations was performed, repeatedly adjusting the values of k_E, k_X, and k_{NMR}. Having found suitable values, longer calculations were performed, employing the four best parameter sets. In these calculations, NMR data were included in the fitting process. For comparison, the same procedure was applied without fitting to NMR data. In total, eight models were generated, four fitted to scattering and NMR data and four fitted only to scattering data. Models that were fitted to scattering and NMR data will be denoted class A models in the following; models that were only fitted to scattering data will be denoted class B models. The values of k_E, k_X, and k_{NMR} that were used in these calculations are listed in table 1.

3. Results and discussion

3.1. Cost functions

To give quantitative insight into the agreement between experimental and calculated data the values of all cost functions are listed in table 2. All cost functions are reduced by about 60–90% during optimization. Particularly good fits are obtained for neutron scattering data. As can be seen in figures 3–5 this is mainly due to a smoother shape of the calculated neutron scattering

Table 2. Starting values and final values of all cost functions. The calculations are labelled according to figures 3–9.

Label	E_{pot} [eV/atom]	CF_{x-ray}	$CF_{neutron}$	$CF_{electron}$	CF_{NMR}
(a)	−5.56	742.8	34.3	523.8	22.2×10^{-4}
Class A: optimization with respect to scattering and NMR data					
(b)	−5.43	237.6	17.0	126.7	4.9×10^{-4}
(c)	−5.32	278.9	11.3	164.8	4.6×10^{-4}
(d)	−5.33	216.4	13.3	132.3	4.5×10^{-4}
(e)	−5.23	226.0	9.8	132.9	4.7×10^{-4}
Class B: optimization only with respect to scattering data					
(f)	−5.63	279.3	26.9	165.0	27.1×10^{-4}
(g)	−5.58	319.3	18.0	177.2	32.0×10^{-4}
(h)	−5.60	262.8	23.2	156.2	28.0×10^{-4}
(i)	−5.55	289.3	16.3	155.4	35.8×10^{-4}

data. The potential energies of models of class A are higher after optimization than before, while all models of class B lie lower in energy.

Generally the values of the cost functions indicate a slightly better agreement with experimental scattering data when the models were fitted to NMR data. Considering the quadratic dependence of the cost function on the deviation these differences are extremely small, though, as can also be seen in figures 3–5.

The effect of the final local optimization, which we included in the optimization procedure to achieve the best possible fit between calculated and experimental data, was a reduction of the cost functions of a few per cent (less than 1% in the case of neutron scattering and NMR data, and 1–7% in the case of x-ray and electron scattering data) relative to the total improvement of the cost function.

3.2. Radial distribution functions and NMR

Figures 3–5 show comparisons between scattering data calculated from the optimized models and experimental data. For comparison, the data of the starting structure are also shown. The two peaks of the radial distribution functions at 1.4 and 1.7 Å can be assigned to B–N and Si–N distances respectively. While the position of the B–N peak remains unchanged during optimization, the Si–N peak is shifted to slightly shorter distances. Generally, the agreement between experimental and calculated data is good. Almost perfect agreement is found for neutron scattering data. The small peak in the x-ray scattering data at 2.1 Å is not reproduced by the models. This peak is most probably an artefact of the Fourier transform of the experimental scattering intensity, an assumption that is supported by results of another series of calculations (not shown here) where we computed $G(r)$ by Fourier transformation of the scattering intensity calculated from the models and were able to perfectly reproduce this peak [30]. Note that there are no differences between the calculated scattering data of class A models (fitted to scattering and NMR data) and class B models (fitted only to scattering data). All radial distribution functions of the starting structure are more roughly shaped and exhibit narrower first-neighbour peaks, which reflects the higher degree of ordering in these structures (cf figure 2).

While the radial distribution functions do not show differences between models of class A and B, the calculated NMR spectra (figure 6) of models of class A and B differ noticeably. Models of class A are in significantly better agreement with experimental ^{15}N NMR data than
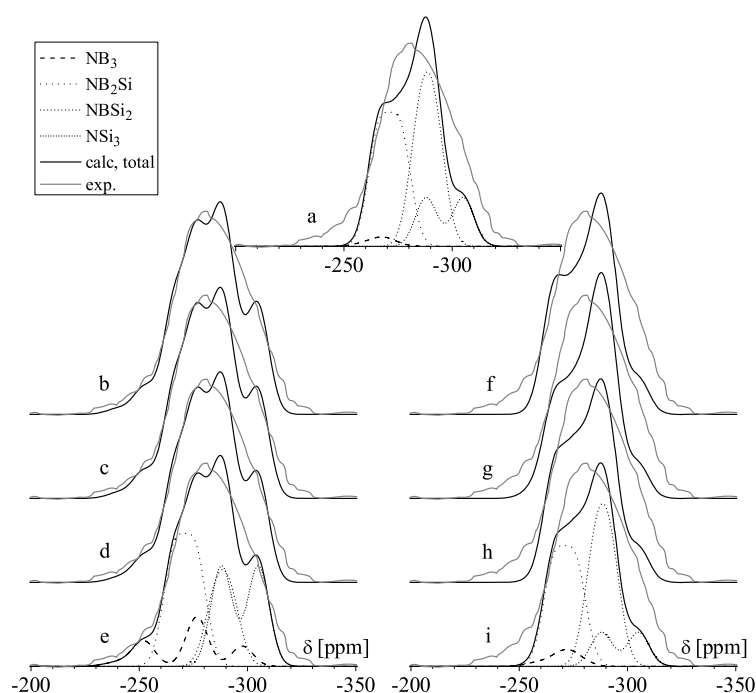
Figure 6. NMR data of optimized models (black) and experimental data (grey) [23]. The sample was 100% ^{15}N enriched. For comparison the data calculated from the starting structure are also shown. In some spectra the partial NMRs (related to different nitrogen environments) are shown. (a) Starting structure; (b)–(e) class A models (optimized with respect to scattering and NMR data); (f)–(i) class B models (optimized only with respect to scattering data).

models of class B, giving a hint that NMR data bring structural information into the models that are not already contained in the radial distribution functions. From the partial NMR spectra shown in figure 6 it can be seen that the differences between the spectra are caused by differences in the distributions of nitrogen coordination environments.

Noteworthy are three peaks observable for NB_3 environments. These correspond to different mean NB distances (-300 ppm: $r_{mean} \approx 1.3$ Å, -250 ppm: $r_{mean} \approx 1.55$ ppm). Because we used a distance-dependent parameterization only for chemical shifts in NB_3 (and NB_4) environments, no such effects are observable for the other coordination environments. However, all peaks are broadened because they are computed as Gaussians.

3.3. Local coordination

Before presenting the results, we make a few remarks about the determination of the coordination environments. Determining coordination environments (which requires the determination of the bond graph) in amorphous structural models is not unambiguous. The usual method of assuming a bond between two atoms if their distance is below a certain element-pair specific threshold is problematic because of the broad distribution of interatomic distances. Using too small thresholds usually generates larger amounts of under-coordinated atoms in the coordination statistic. Enlarging the threshold reduces the number of under-coordinated atoms but increases the fraction of over-coordinated atoms. We decided to use
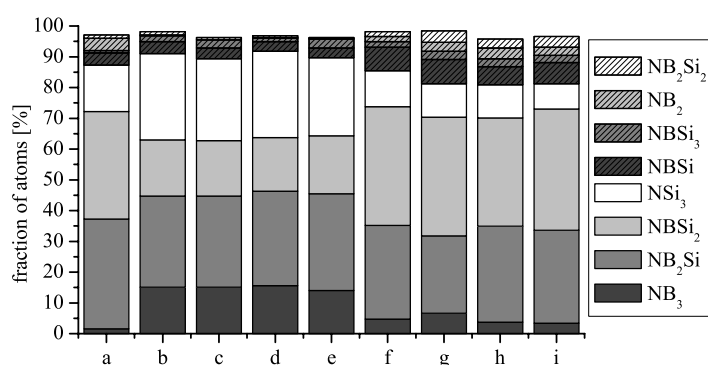
Figure 7. Fractions of N atoms in different coordination environments. (a) Starting structure; (b)–(e) class A models (optimized with respect to scattering and NMR data); (f)–(i) class B models (optimized only with respect to scattering data).

a procedure for determination of the bond graph that is in line with chemical intuition which expects bonds between spatially near atoms with unsaturated valencies. The procedure shall be outlined in the following. In a first loop over all atoms, bonds were created applying element-pair specific distance thresholds. In a second loop we tried to reduce the numbers of under- and over-coordinated atoms. If an atom was under-coordinated (assuming correct coordination numbers of 3 for B and N and 4 for Si), we looked for under-coordinated atoms within the 1.1 fold of the distance threshold and created a bond between the nearest of these atoms and the current atom under consideration. Accordingly, for over-coordinated atoms, we searched the first coordination sphere for atoms that were also over-coordinated and broke the bond to the farthest of them if it was not nearer than the 0.9 fold of the distance threshold. Up to this point, this correction procedure did not account for donor–acceptor bonds which are possible between B and N. These were created in the last loop where only up to threefold coordinated B and N atoms were considered. If a possible bonding partner (B for N and vice versa) was found within the 1.1 fold of the distance threshold, a donor–acceptor bond was created (if several possible bonding partners were found, the nearest of them was bonded). Our algorithm implies that donor–acceptor bonds are preferably created between atoms that are farther apart, while covalent bonds are preferably created between spatially nearer atoms, reflecting the observation that donor–acceptor bonds are usually longer and weaker than covalent bonds.

As was already visible in the NMR spectra, the distributions of coordination environments clearly show differences between models that were optimized with (class A) and without inclusion of NMR data (class B). Naturally, these differences are mainly found in the distribution of nitrogen environments (figure 7). Models of class A contain mostly NSi_3 and NB_2Si environments in roughly equal amounts (about 30%). NB_3 and $NBSi_2$ environments are also found, but in lower fractions of about 15 to 20%. Models of class B contain mostly $NBSi_2$ and NB_2Si environments. Besides these chemically 'correct' coordination environments, all models including the starting structure contain minor amounts of under- and over-coordinated nitrogen shells like $NBSi$ and $NBSi_3$. The amount of these environments is slightly lower in the structures which were optimized with respect to NMR data. Interestingly, this is not the case in class B models. Despite the changes of scattering data during the optimization, the composition of nitrogen environments remains nearly unchanged in models that were only optimized with respect to scattering data. Obviously NMR data bring structural information into the model that may not be gained from scattering data alone.
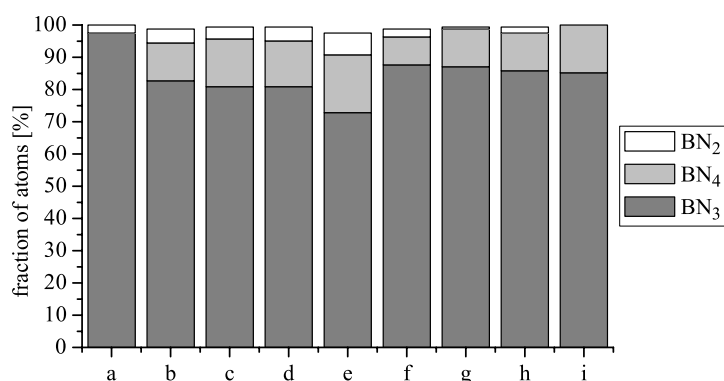
Figure 8. Fractions of B atoms in different coordination environments. (a) Starting structure; (b)–(e) class A models (optimized with respect to scattering and NMR data); (f)–(i) class B models (optimized only with respect to scattering data).
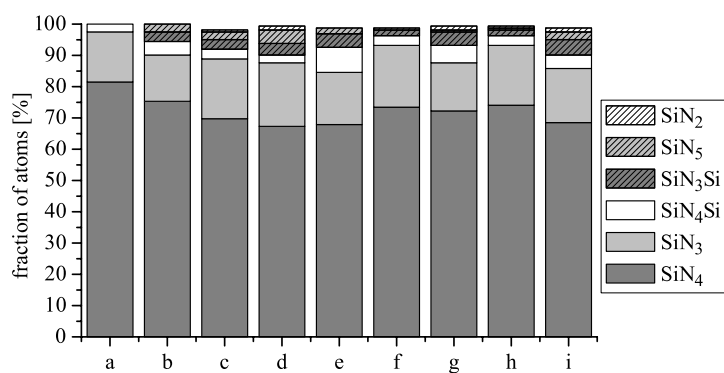

Figure 9. Fractions of Si atoms in different coordination environments. (a) Starting structure; (b)–(e) class A models (optimized with respect to scattering and NMR data); (f)–(i) class B models (optimized only with respect to scattering data).

The distributions of B and Si coordination environments do not show significant differences between models of class A and B (figures 8 and 9). All models contain mostly threefold coordinated boron in BN_3 environments, in agreement with experimental ^{11}B NMR data. Besides these environments all optimized models contain smaller fractions of boron in BN_4 environments as well as very small amounts of under-coordinated boron in BN_2 environments. The presence of smaller amounts of BN_4 environments in the ceramic could not be excluded from the ^{11}B NMR measurements in [23] because the experimental signal was broadened due to quadrupole effects so that the peak partially ranged up to the zone where signals of BN_4 units are expected. Very recent multiple quantum MAS NMR experiments, however, confirmed that there are only BN_3 environments present in the ceramic [37]. The majority of silicon atoms is surrounded by four nitrogen atoms, which is in agreement with the ^{29}Si NMR spectrum, but there are also smaller amounts of under-coordinated silicon in SiN_3 environments. Some silicon atoms are surrounded by more than four neighbours.

3.4. Second-nearest neighbours and rings

Amorphous $Si_3B_3N_7$ is composed of SiN_4- and BN_3-units which are connected by either boron or silicon. The numbers of B and Si atoms in the second coordination sphere of silicon and

13

Table 3. Mean numbers of second-nearest neighbours of B and Si in the starting structure and in optimized models of class A (optimized with respect to scattering and NMR data) and B (optimized only with respect to scattering data). Also shown are the experimentally determined values. Last column: values that are expected for purely statistical connection without preference for certain bonding schemes. B–X–Si means Si atoms in the second coordination sphere of B. The labelling of the other second neighbours follows the same rules.

	Starting structure	Class A	Class B	Exp. [24]	Stat.
B–X–B	2.6 ± 0.4	3.6 ± 0.2	2.7 ± 0.1	4.5 ± 0.5	2.6
B–X–Si	3.7	3.1 ± 0.2	4.1 ± 0.2	1.4 ± 0.2	3.4
$\sum$	6.3 ± 0.4	6.6 ± 0.4	6.8 ± 0.3	5.9 ± 0.7	6.0
Si–X–B	3.7	3.2 ± 0.3	4.1 ± 0.3	1.8 ± 0.1	3.4
Si–X–Si	4.1 ± 0.2	4.8 ± 0.2	4.3 ± 0.3	6.5 ± 0.5	4.6
$\sum$	7.8 ± 0.2	8.0 ± 0.5	8.4 ± 0.6	8.3 ± 0.6	8.0

boron thus give information about preferred connectivities of these building units and also about the homogeneity of the spatial distributions of Si and B in the ceramic. Experimentally, the numbers of second Si and B neighbours of silicon and boron were determined from a series of double resonance NMR experiments [24]. From these experimental data (see table 3) it was concluded that the distribution of silicon and boron is not homogeneous. Instead, there must be regions with increased silicon or boron content. The size of these regions of inhomogeneity must however be limited to $\approx$10 Å as was shown by TEM experiments [22], so that the size of our models is sufficient to reproduce such inhomogeneities.

Because the experimental second-nearest-neighbour data were not included in the fitting process they might also serve as an interesting test of our models. Investigations by Hannemann *et al* had shown that is difficult to reach good agreement with experimental second-nearest-neighbour data [17–19]. These authors generated several structural models of a-$Si_3B_3N_7$, employing several building schemes, partly followed by reverse Monte Carlo refinements. Especially one class of their models, which were based on starting structures very similar to the one used in this work, exhibited large deviations of the second-nearest-neighbour statistics from the experimental values.

Before discussing the results, some remarks about the determination of the second-nearest neighbours from our structures are appropriate. In principle, the numbers of second-nearest neighbours may be determined either from the bond graph or from the partial radial distribution functions by integration over the peak of the second coordination sphere. Because the experimental values of the second-nearest neighbours were evaluated by a distance-based analysis of the experimental data, we also calculated the numbers of second-nearest neighbours from the radial distribution functions. For this purpose we integrated over the second-neighbour peaks of the partial radial distribution functions taking the first minimum after the second-neighbour peak (there was always an overlap of the second-neighbour peaks with peaks of higher coordination spheres) as the upper integration limit. In some cases, this minimum was not clearly defined and we performed several integrations varying the upper integration limit. This is indicated by the error limits in table 3.

As can be seen in table 3, there are still significant deviations between the numbers of second neighbours calculated from the models and the values determined from experimental NMR data. However, fitting to NMR data in addition to scattering data clearly improves the quality of the models. It should be remembered that the scattering data of all optimized models are very similar; thus the differences of the numbers of second neighbours are a consequence
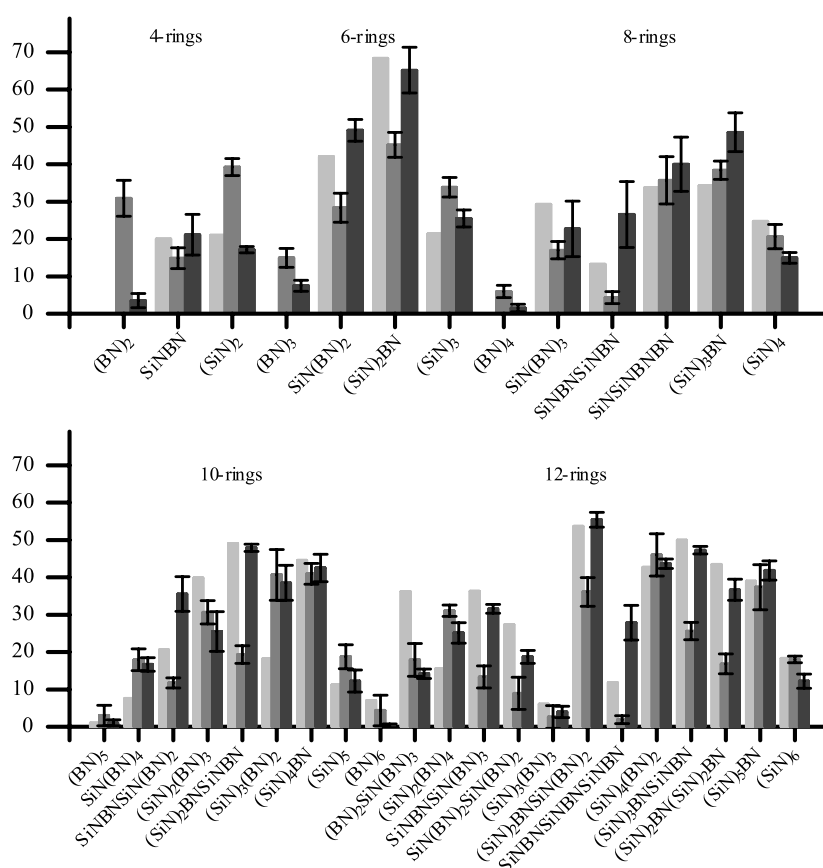
Figure 10. Numbers of rings of different compositions. Light grey: starting structure; grey: class A models (optimized with respect to scattering and NMR data); dark grey: class B models (optimized only with respect to scattering data). Except for the starting structure the values are mean values over different models. Bars indicate the variation range within a class.

of the inclusion of NMR data in the fitting process. Fitting to NMR data modifies the fractions of different nitrogen environments in the model and thus the connectivity of the SiN_4 and BN_3 units. In models that were only fitted to scattering data the numbers of second neighbours remain basically unchanged during the optimization process. The sums of second-nearest neighbours (especially of boron) are somewhat higher than the ideal values of 6 (for B) and 8 (for Si) which are based on the assumption that there are only BN_3 and SiN_4 building units. This is due to deviations from the ideal bonding scheme in the models and does not change the observed trend that fitting to the ^{15}N NMR spectrum favours B–N–B– and Si–N–Si–linkages.

In order to gain quantitative insight into structural features beyond the first two coordination spheres we performed a ring analysis (figure 10). Rings of different compositions (for example 4-rings with compositions $(SiN)_2$ and SiNBN) were treated separately. The search for rings of a certain composition was performed by looking for all closed loops over the bond graph with the corresponding sequence of atoms. Sets of atoms defining smaller rings were not allowed to contribute as a whole to a larger ring.

All models contain significant numbers of 4-rings, which are predominantly pure $(BN)_2$ and $(SiN)_2$ rings in class A models. In class B models the numbers of 4-rings remain essentially
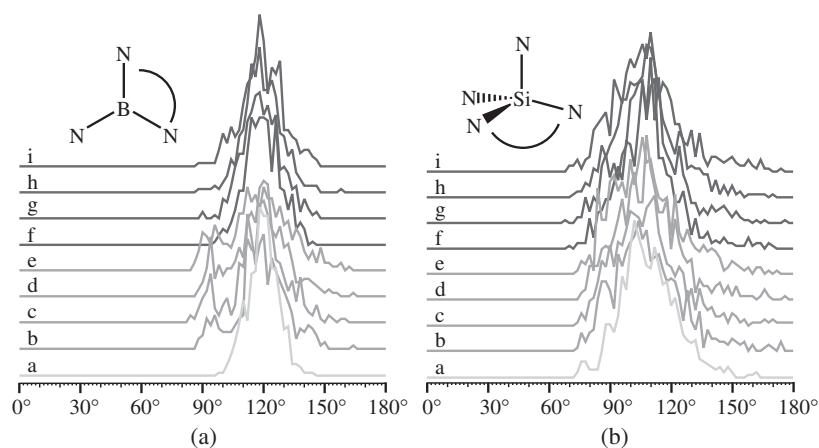
Figure 11. Distributions of bond angles N–B–N and N–Si–N in BN$_3$ and SiN$_4$ coordination environments in the starting structure and in optimized models of class A (optimized with respect to scattering and NMR data) and B (optimized only with respect to scattering data). All distribution functions are normalized to the total number of angles of that type in a model. (a) Starting structure; (b)–(e) class A models; (f)–(i) class B models.

the same as in the starting structure. The diagonal distances in these rings correspond to small peaks around 2 Å in the radial distribution functions. A favouring of homogeneous (SiN)$_6$ and (BN)$_6$ rings over mixed (SiN)$_x$(BN)$_y$ rings in class A models compared to class B models is still apparent in the statistics of 6-rings. However, the majority of 6-rings are mixed rings like SiN(BN)$_2$, especially in models of class B. Even larger pure rings (BN)$_n$ ($n = 4, 5, 6$) are found, favourably in models of class A. These pure rings become less important with increasing ring sizes where the majority of atoms is involved in mixed rings. The total numbers of rings with sizes $\geqslant 6$ are larger in class B models than in class A models, whereas small 4-rings are predominantly found in class A models. The results shown in figure 10 show that inclusion of NMR data in the fitting process does not only affect short-range structural features like coordination environments but also larger structural elements like rings. The latter is of course a consequence of the effect on the coordination environments.

3.5. Bond angles and distribution of distances

More insight into the local structures around the atoms in the models can be gained from the bond angle distributions. We analysed the distributions of bond angles separately for different coordination environments considering the most frequent coordination environments. The distributions of the bond angles around the two building units of the ceramic (BN$_3$ and SiN$_4$) are shown in figure 11. Figures of bond angle distributions in other coordination environments are provided as supplementary material (available at stacks.iop.org/JPhysCM/19/056201).

All models exhibit relatively broad distributions of bond angles. Maxima of the bond angle distribution in threefold B and N coordination environments are found at $\approx 120°$, corresponding to a trigonal planar coordination environment. SiN$_4$ environments have a maximum of the bond angle distribution at $\approx 110°$, as is expected for a tetrahedral coordination. Interestingly the bond angles in SiN$_3$ environments are also distributed around $\approx 110°$, which indicates that the coordination is mainly non-planar in these environments. The shoulders and peaks in the bond angle distributions at $\approx 90°$ are consistent with the presence of 4-rings which were discussed in section 3.4. No angles around 60°, which are typical for small 3-rings, are visible in the distributions of bond angles.
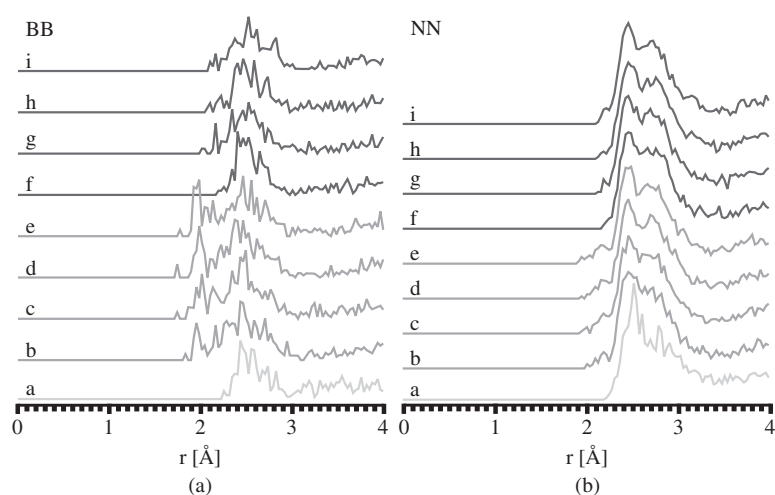
Figure 12. Partial radial densities $\rho_{BB}(r)$ and $\rho_{NN}(r)$ of the starting structure and of optimized models of class A (optimized with respect to scattering and NMR data) and B (optimized only with respect to scattering data). (a) Starting structure; (b)–(e) class A models; (f)–(i) class B models.
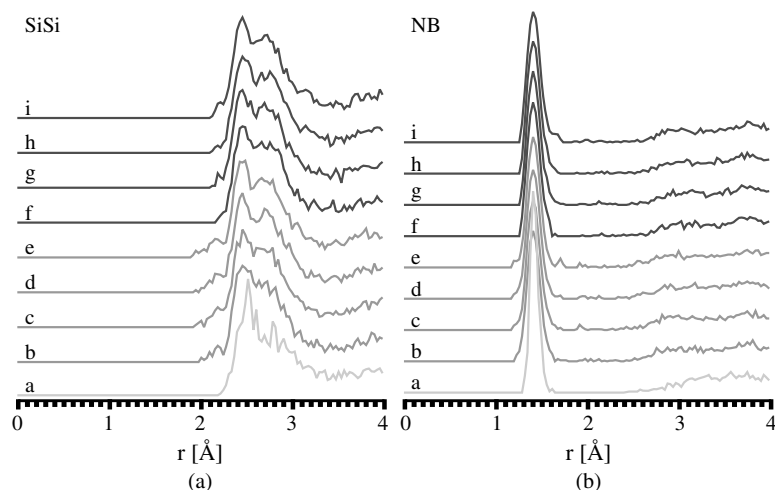

Figure 13. Partial radial densities $\rho_{SiSi}(r)$ and $\rho_{NB}(r)$ of the starting structure and of optimized models of class A (optimized with respect to scattering and NMR data) and B (optimized only with respect to scattering data). (a) Starting structure; (b)–(e) class A models; (f)–(i) class B models.

Distance distributions between pairs of elements A and B were examined by calculating the radial densities $\rho_{AB}(r)$ (the mean particle densities of atoms of type B in a distance r from an atom of type A) which are shown in figures 12–14. For better readability the functions are only shown up to 4 Å. The y-scale is identical in all figures.

From these functions it can be seen that the two peaks at 1.4 and 1.7 Å in the total RDFs are related to B–N and Si–N distances, respectively. The second-neighbour peaks at 2.5 and 2.8 Å are mainly related to Si–Si and N–N distances and to a lower extend also to B–B and Si–B distances. The diagonal distances in small 4-rings, which are predominantly found in class A models and which are also visible in the distributions of bond angles, are related to
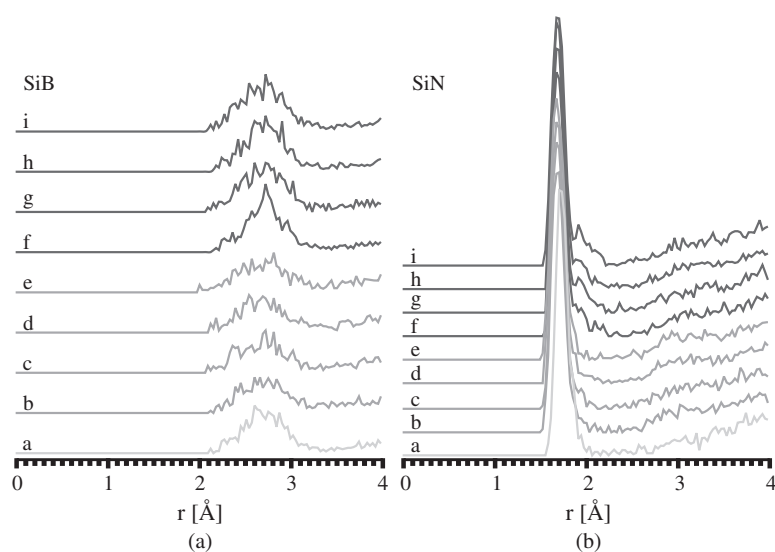
17

Figure 14. Partial radial densities $\rho_{SiB}(r)$ and $\rho_{SiN}(r)$ of the starting structure and of optimized models of class A (optimized with respect to scattering and NMR data) and B (optimized only with respect to scattering data). (a) Starting structure; (b)–(e) class A models; (f)–(i) class B models.

smaller peaks at ≈ 2 Å in the B–B radial density and ≈ 2.2 Å in the N–N radial density. The small shoulder at ≈ 2.2 Å in the Si–Si radial density may be assigned either to diagonal Si–Si distances in $(SiN)_4$ rings but more probably to directly bonded Si atoms, because Si–Si distances in $(SiN)_4$ rings are typically larger. Beside these differences all radial densities are very similar in models of class A and B.

Comparing the relatively narrow first-neighbour peaks of $\rho_{NB}(r)$ and $\rho_{SiN}(r)$ one finds that the distribution of the first-neighbour distances is slightly broadened in all optimized structures compared to the starting structure which might be due to the calculation of the scattering data in real space. In addition to this broadening the Si–N first-neighbour peak is shifted to slightly shorter distance after optimization while the position of the N–B first-neighbour peak remains constant.

3.6. Free volume

The average density of our models is 2.5 g cm^{-3}, which is much larger than the surprisingly low experimental density of 1.9 g cm^{-3} of a-Si$_3$B$_3$N$_7$ powder [38]. At the beginning of our investigations we performed some shorter optimizations with scaled models that had the correct density of 1.9 g cm^{-3}, but with these models it was very difficult to achieve reasonable agreement with experimental data, so we decided to use the model with the larger density. At first sight this might seem questionable, but comparing this density with the averaged densities of crystalline h-BN ($\rho = 2.34$ g cm^{-3} [39]) and Si$_3$N$_4$ ($\rho(\alpha$-Si$_3$N$_4) = 3.18$ g cm^{-3}, $\rho(\beta$-Si$_3$N$_4) = 3.20$ g cm^{-3} [40]) of 2.83 g cm^{-3}, the model density is reasonable.

Already by visual inspection voids were detectable in the optimized structures, indicating that the local density even increased during optimization. To put this observation on a more quantitative basis we measured the free volumes of the structures by scanning them with test spheres with varying diameters. The scanning was carried out on a grid with a resolution of 0.05 Å. At each point of this grid the distance of the centre of the test sphere to all surrounding atomic centres was calculated. If this distance was larger than the sum of the test sphere radius
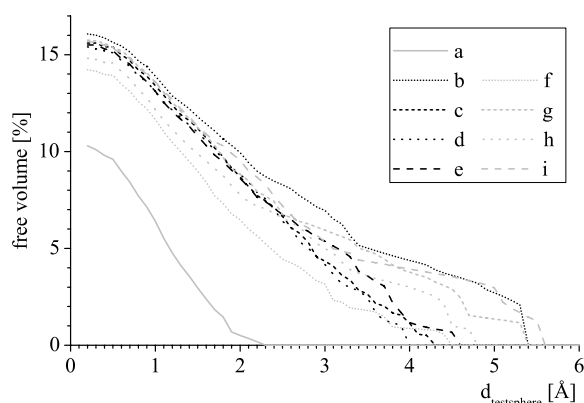
Figure 15. Free volume V_{free} (d) as fraction of the simulation cell volume for different diameters d of the test sphere. (a) Starting structure; (b)–(e) class A models (optimized with respect to scattering and NMR data); (f)–(i) class B models (optimized only with respect to scattering data).

plus the atomic van der Waals radius for all atoms, all grid points belonging to the test sphere were marked as part of the free volume. After applying this procedure to all grid cells, the free volume was determined by counting all grid cells that were marked as free. The scanning was repeated using different radii of the test sphere.

The volumes $V_{free}(d)$ that were accessible for test spheres with varying diameters d are shown in figure 15. $V_{free}(d)$ is monotonically falling for all structures, indicating that the shapes of the voids are not compact but rather dendritic: for small diameters of the test sphere, a net of narrow voids is detectable, seaming the whole structure. With increasing diameter the voids become more compact and separated. The largest voids calculated with this set of van der Waals radii have diameters between 4 and 6 Å in the optimized structures and about 2 Å in the starting structure (one must however keep in mind that the absolute size of the voids depends on the chosen size of atomic radii, which are to a certain degree arbitrary). The shapes of V_{free} (d) of the optimized structures differ slightly, showing no systematic differences between models of classes A and B. However, all free volumes of the optimized structures are larger than in the starting structure, indicating that the occupied regions of the models shrink during optimization and that the density in these regions exceeds the mean density of 2.5 g cm^{-3}. We tried to detect the local densities in the non-void regions of our models by measuring the density in spherical volume elements with diameters of a few Å. An exact determination of the density of the non-void regions was hampered by the fact that these regions had dimensions of only a few Å. On such small length scales the density is ill defined, resulting in a strong dependence of the calculated local densities on the radius of the volume element used for density measurement. Probing the local densities using spherical volume elements with radii between 3 and 4 Å, we obtained mean densities of the occupied regions of about 2.9–3.1 g cm^{-3} (calculated from the mean values of the local density in regions with increased local density) which is comparable to the densities of the hypothetical crystalline structures of Kroll and Hoffmann [33] of 2.8–2.9 g cm^{-3}. This result supports the hypothesis of Hannemann *et al* that the surprisingly low experimental density of a-Si$_3$B$_3$N$_7$ can be explained by the presence of small voids generated during the synthesis which are surrounded by regions with higher density [18, 7].

4. Summary and conclusion

We have presented a modification of the reverse Monte Carlo method that allows for fitting of the structural model to NMR spectra in addition to scattering data. Using this method and

data from previous theoretical investigations of NMR chemical shifts [11, 26, 25, 27] it was for the first time possible to generate structural models of a-$Si_3B_3N_7$ which are not only in agreement with scattering data from three different experimental sources (x-ray, neutron and electron scattering) but also with the ^{15}N NMR spectrum of the ceramic. An interpretation of this spectrum was not possible before since it exhibits a broad structureless peak that is a superposition of signals related to different nitrogen environments whose chemical shifts were only partly known experimentally.

Fitting to the ^{15}N NMR spectrum affects the fractions of different N coordination environments in the models. These structural effects are not visible in the radial distribution functions of the models, showing the necessity of including further information than experimental scattering data in the fitting process. Because N connects the BN_3 and SiN_4 building units of the ceramic, changes in the nitrogen coordination environments also change the preferred connection scheme of these building units. As a result, the numbers of second-nearest B and Si neighbours of B and Si were more similar to the experimental values when the models were fitted to the NMR spectrum. There are, however, still significant deviations between the calculated and the experimentally determined numbers of second neighbours. The results of Hannemann *et al* [18] show that the numbers of second-nearest neighbours in the models depend on the starting structure of the optimization process, so these deviations could probably be reduced by using other starting structures. They possibly also could be reduced if better parameterizations of the chemical shifts were available (see below).

In all structural models voids can be detected after RMC optimization, indicating that the local density in the non-void regions is even higher than the mean density of 2.51 g cm^{-3}. This is a hint that the surprisingly low experimental density of 1.9 g cm^{-3} can be explained by the presence of small voids surrounded by regions with higher density, as was already proposed by Hannemann *et al* [18, 7].

The currently used parameterizations for calculation of the chemical shifts during optimization are rather crude. It would be highly desirable to have parameterizations at hand that take more detailed structural features into account. This would further improve the reliability of the models. From our experience it is, however, not easy to develop such a parameterization for solid state chemical shifts.

Acknowledgments

References

[1] Jansen M and Baldus H-P 1997 Novel high-performance ceramics—amorphous inorganic networks from molecular precursors *Angew. Chem. Int. Edn* **36** 328–43

[2] Baldus H-P, Jansen M and Sporn D 1999 Ceramic fibers for matrix composites in high-temperature engine applications *Science* **285** 699–703

[3] Jansen M, Jäschke B and Jäschke T 2002 Amorphous multinary ceramics in the Si–B–N–C system *Structure and Bonding* vol 101 *High Performance Non-Oxide Ceramics* ed M Jansen (Berlin: Springer) pp 137–92

[4] Kroll P 2005 Modelling polymer-derived ceramics *J. Eur. Ceram. Soc.* **25** 163–74

[5] Matsunaga K and Iwamoto Y 2001 Molecular dynamics study of atomic structure and diffusion behaviour in amorphous silicon nitride containing boron *J. Am. Ceram. Soc.* **84** 2213–9

[6] Hannemann A, Schön J C, Jansen M and Sibani P 2005 Nonequilibrium dynamics in amorphous $Si_3B_3N_7$ *J. Phys. Chem.* B **109** 11770–6

[7] Hannemann A, Schön J C and Jansen M 2005 Stability of nanovoids in amorphous $Si_3B_3N_7$ *Phil. Mag.* **85** 2621–39

[8] Wefing S 1999 Modeling of continuous random networks: a case study for vitreous GeO_2. I. Model generation *J. Non-Cryst. Solids* **244** 89–111

[9] Wefing S 1999 Modeling of continuous random networks: a case study for vitreous GeO_2. II. Topological analysis and refinement *J. Non-Cryst. Solids* **244** 112–27

[10] Gastreich M and Marian C M 1998 *Ab initio* prediction of ^{15}N-NMR chemical shift in α-boron nitride based on an analysis of connectivities *J. Comput. Chem.* **19** 716–25

[11] Marian C M and Gastreich M 2001 Quantitative structure–property relationships in boron nitrides: the ^{15}N- and ^{11}B chemical shifts *Solid State NMR* **19** 29–44

[12] Reinhardt S, Gastreich M and Marian C M 2002 Quantum chemical investigation of initial reactions between the molecular precursor TADB and ammonia. 1. Gas-phase reactions *J. Phys. Chem.* A **106** 4205–16

[13] McGreevy R L and Pusztai R L 1988 Reverse Monte Carlo simulation: a new technique for the determination of disordered structures *Mol. Simul.* **1** 359–67

[14] McGreevy R L 2001 Reverse Monte Carlo modelling *J. Phys.: Condens. Matter* **13** 877–913

[15] Zwanziger J W 1998 Structure and chemical modifications in oxide glasses *Int. Rev. Phys. Chem.* **17** 65–90

[16] McLaughlin J C, Tagg S L, Zwanziger J W, Haeffner D R and Shastri S D 2000 The structure of tellurite glass: a combined NMR, neutron diffraction, and x-ray diffraction study *J. Non-Cryst. Solids* **274** 1–8

[17] Hannemann A, Schön J C, Jansen M, Putz H and Lengauer T 2004 Modelling amorphous $Si_3B_3N_7$: structure and elastic properties *Phys. Rev.* B **70** 144201

[18] Schön J C, Hannemann A and Jansen M 2004 Modelling the synthesis of amorphous $Si_3B_3N_7$ via a sequence of dynamically well-separated steps *J. Phys. Chem.* B **108** 2210–7

[19] Hannemann A, Schön J C and Jansen M 2005 Modeling the sol–gel synthesis route of amorphous $Si_3B_3N_7$ *J. Mater. Chem.* **15** 1167–78

[20] Hagenmayer R M, Müller U, Benmore C J, Neuefeind J and Jansen M 1999 Structural studies on amorphous silicon boron nitride $Si_3B_3N_7$: neutron contrast technique on nitrogen and high energy x-ray diffraction *J. Mater. Chem.* **9** 2865–70

[21] Hagenmayer R M, Müller U and Jansen M 2000 Neutron contrast technique on nitrogen in $Si_3B_3N_7$ *Physica* B **276** 423–4

[22] Heinemann D, Assenmacher W, Mader W, Kroschel M and Jansen M 1999 Structural characterization of amorphous ceramics in the system Si–B–N–(C) by means of transmission electron microscopy methods *J. Mater. Res.* **14** 3746–53

[23] Müller U, Hoffbauer W and Jansen M 2000 Short-range ordering in amorphous $Si_3B_3N_7$ as determined by multinuclear NMR spectroscopy *Chem. Mater.* **12** 2341–6

[24] van Wüllen L, Müller U and Jansen M 2000 Understanding intermediate-range order in amorphous nitridic ceramics: A ^{29}Si{^{11}B} REDOR/REAPDOR and ^{11}B{^{29}Si} REDOR study *Chem. Mater.* **12** 2347–52

[25] Gastreich M 2001 Tools zur Modellierung von Siliciumbornitridkeramiken: Entwicklung von Mehrkörperpotenzialen und Berechnungen zur NMR-chemischen Verschiebung *PhD Thesis* University of Bonn http://hss.ulb.uni-bonn.de/diss_online/math_nat_fak/2001/gastreich_marcus

[26] Gastreich M, Doerr M and Marian C M, Assessment of cluster sizes, connectivities and sizes to foresee ^{15}N chemical shifts in silicon nitrides, in preparation

[27] Doerr M and Marian C M 2006 The ^{15}N chemical shifts in mixed NB_2Si and $NBSi_2$ environments of $Si_3B_3N_7$—a theoretical investigation *Solid State NMR* **30** 16–28

[28] Kirkpatrick S, Gelatt C D and Vecchi M P 1983 Optimization by simulated annealing *Science* **220** 671–80

[29] Kirkpatrick S 1984 Optimization by simulated annealing—quantitative studies *J. Stat. Phys.* **34** 975–86

[30] Doerr M 2006 Strukturmodellierung amorpher Festkörper–Entwicklung eines erweiterten reverse-Monte-Carlo-Programms und Untersuchungen zu NMR-chemischen Verschiebungen in Festkörpern *PhD Thesis* University of Düsseldorf http://diss.ub.uni-duesseldorf.de/ebib/diss/show?dissid=1461

[31] Jeschke G, Hoffbauer W and Jansen M 1998 A comprehensive NMR study of cubic and hexagonal boron nitride *Solid State NMR* **12** 1–7

[32] Harris R K, Leach M J and Thompson D P 1990 Synthesis and magic-angle spinning nuclear magnetic resonance of ^{15}N-enriched silicon nitrides *Chem. Mater.* **2** 320–3

[33] Kroll P and Hoffmann R 1998 Silicon boron nitrides: hypothetical polymorphs of $Si_3B_3N_7$ *Angew. Chem. Int. Edn* **37** 2527–30

[34]　Massiot D, Fayon F, Capron M, King I, Le Calvé S, Alonso B, Durand J-O, Bujoli B, Gan Z and Hoatson G 2002 Modelling one- and two-dimensional solid-state NMR spectra *Magn. Res. Chem.* **40** 70–6

[35]　Marian C M, Gastreich M and Gale J D 2000 Empirical two-body potential for solid silicon nitride, boron nitride, and borosilazane modifications *Phys. Rev.* B **62** 3117–24

[36]　Oligschleger C 2003 personal communication, University of Applied Sciences Bonn–Rhein–Sieg

[37]　Jansen M, Schön J C and van Wüllen L 2006 The route to the structure determination of amorphous solids: a case study of the ceramic $Si_3B_3N_7$ *Angew. Chem. Int. Edn* **45** 4244–63

[38]　Jäschke T 2002 Hochtemperaturstabile Si/B/N/C-Keramiken aus neuen Einkomponentenvorläufern *PhD Thesis* University of Bonn

[39]　Mishima O and Era K 2000 Science and technology of boron nitride *Electric Refractory Materials* ed Y Kumashiro (New York: Dekker) pp 495–556

[40]　Wang C-M, Pan X, Rühle M, Riley F L and Mitomo M 1996 Silicon nitride crystal structure and observations of lattice defects *J. Mater. Sci.* **31** 5281–98